




A Novel Rotating Flexure-Test Technique for Brittle Materials with Circular Geometries

M. Maclsaac¹ · S. Bavdekar¹ · J. Nance² · B. Sankar¹ · N.-H. Kim¹ · G. Subhash¹ 

Received: 20 October 2021 / Accepted: 1 March 2022
© The Society for Experimental Mechanics, Inc 2022

Abstract

The four-point bend test is one of the simplest and often the preferred flexural strength evaluation method for brittle materials. In this loading mode, fracture often initiates from a critical surface (or subsurface) flaw when subjected to a tensile stress state. However, if the critical flaw exists on the compression side of the test specimen, it may not activate to grow a crack and hence the resulting flexural strength will be higher than the true value. The goal of this study is to measure the true flexural strength of a solid or hollow cylindrical brittle specimen by ensuring that failure occurs at its weakest point by rotating along its longitudinal axis, thereby exposing and activating its critical surface flaw during a four-point bend test. A novel test fixture has been designed and fabricated, and the true flexural strengths of cylindrical brittle and quasi-brittle tubular specimens have been measured and compared to existing experimental data obtained through traditional four-point bend tests. Experimental results showcase the orientation dependence on flexural strength for various materials. Additionally, similarities between experimental findings and those available in literature, including observations of fracture surfaces and relationships between surface roughness and material strength, are discussed.

Keywords Rotating four-point bend test · Critical flaw · Brittle fracture · Borosilicate glass

Introduction

Brittle materials, such as ceramics, are favorable candidates for use in harsh environments due to their high melting temperature, high hardness, high strength, and good chemical and wear resistance [1–3]. Unlike ductile materials, failure in brittle materials is governed by their inherent microstructural inhomogeneities [4] and evaluating their strength using the conventional tensile test is not always preferred because of the difficulty in machining a dog-bone shaped test specimen without surface defects. The machining induced surface defects can cause premature failure during loading. In addition, designing an appropriate specimen mounting fixture that does not deleteriously influence the failure mode in the gage section is also challenging as it may cause undue stress concentration in the grips and activate crack propagation

from nearby defects. Because of these difficulties, a flexural test is often the preferred strength evaluation method for brittle materials as it requires no specimen gripping and simple geometries, such as uniform rectangular or circular cross-sectional beams, can be used [5].

However, conventional flexural tests, either in the three-point or four-point bend configuration [6], have a few limitations. The failure strength of a ceramic specimen is often a function of a critical surface or subsurface flaw, and only those flaws that experience the maximum tensile stress activate to grow cracks under the applied loads [3, 4]. In a conventional flexural test with a rectangular cross-section specimen, only one surface of the material experiences the maximum tensile stress. Only the flaws that exist on this surface are activated to grow into larger cracks that eventually induce failure. If the critical flaw exists elsewhere on the specimen surface (e.g., on a compression side), it will not be activated and hence, the measured strength will be higher than the true flexural strength of the specimen material.

This situation is further exacerbated if the test specimen has a cylindrical geometry because the maximum tensile stress occurs along a single line during conventional flexural loading, as compared to a plane for a rectangular prismatic

✉ G. Subhash
subhash@ufl.edu

¹ Mechanical and Aerospace Engineering, University of Florida, Gainesville, FL 32611, USA

² Material Science and Engineering, University of Florida, Gainesville, FL 32611, USA



specimen. Therefore, the probability of a critical flaw existing on this maximum tensile stress line is further diminished and the flexural strength values obtained from testing a few cylindrical specimens could be more prone to scatter, and well above the conservative strength values.

To remedy this situation, we have developed a novel rotating four-point bend test fixture which exposes the entire surface of a cylindrical specimen to the maximum tensile stress, thus increasing the probability (and potentially ensuring) that failure occurs at its critical surface flaw. This is achieved by rotating the cylindrical specimen along its longitudinal axis throughout the duration of a four-point bend test. In Section 2, the design details of the test fixture are described followed by descriptions of tests on a few brittle and quasi-brittle materials with different surface conditions in Section 3. The results of these tests and discussions are presented in Section 4 and conclusions are drawn in Section 5.

Test Fixture Design

The design of the rotating bend-test fixture consists of several features: ease of specimen mounting and loading, control of specimen rotational speed, low specimen torsion, minimum test fixture vibrations, and the ability to adapt to standard loading frames on universal testing machines (UTMs). The fixture, rendered in Fig. 1, consists of two assemblies: a lower assembly to support and rotate the specimen, and an upper assembly to engage the specimen and apply the load. Both assemblies, shown in Fig. 2(a), are designed to be accommodated in an Instron® model 5969 UTM (Norwood, MA, USA) for support and load application. In a standard four-point bend fixture [6], the specimen rests on two fixed outer support anvils and the load is applied via two inner loading anvils. In this fixture, the specimen is cradled between four pairs of aluminum rollers mounted on four separate shafts. The two pairs of lower rollers constitute the outer span (120 mm), and the two pairs of upper rollers constitute the inner span (40 mm) of the flexural loading fixture. One of the bottom shafts is the driveshaft, and is connected through a gearbox (AutomationDirect, Inc. model PGCN23-2525) to an encoded servo motor (Teknic, Inc., model CPM-MCVC-2311 S-RQN).

The specimen is placed between the two pairs of lower rollers, as shown in Fig. 2(b), and the upper frame is slowly lowered to apply the quasistatic four-point flexure loading. As the drive shaft rotates, the specimen is rotated due to friction between the rollers and the specimen surface after a small preload of ~ 10 N is applied. It is important to note that specimen rotation is accomplished via two powered rollers that contact the specimen at its two ends. While torsion may exist due to elastic twist of this drive shaft which may cause differential rotational speeds of the rollers, such

differential speeds are expected to be small as the applied loads are relatively low and the powered rollers are mounted on a single, steel drive shaft. Hence the generated torsion is minimal and can be neglected (supporting calculations can be found in Section 4.1). The remaining six rollers are free rollers. While some friction arises due to the rolling resistance between these rollers and the specimen, this resistance is necessary for specimen rotation and its contribution to specimen torsion and failure is considered negligible as later calculations and failure surface analysis both indicate bending dominated failure. Due to slippage, the rotational speed of the specimen is different from the rotational speed of the driveshaft. To accurately measure the specimen speed, a lightweight 3D printed propeller is attached to the end of the specimen (away from the rollers) and the propeller blades are positioned to pass through a photoelectric fork sensor (AutomationDirect model PSUR-0 N-3 F, Cumming, GA, USA), as shown in Fig. 2(c). The rotational speed of the specimen is calculated based on the number of times a propeller blade passes through the fork sensor within a given time. A single-board microcontroller (Arduino® Mega 2560 REV3) interprets the speed calculated from the fork sensor to adjust the rotational speed of the specimen dynamically. This speed is a set value, typically between 80 and 200 rpm.

The applied load, the upper frame displacement, and the rotational speed of the specimen are monitored during the test until the specimen fails. The flexural strength of each cylindrical specimen is calculated as

$$\sigma_f = \frac{P_{max}(L_o - L_i)r_o}{4I} \quad (1)$$

where, P_{max} is the maximum load applied (at failure) by the UTM; L_o and L_i are the support spans of the outer and inner rollers, respectively; r_o and r_i are the outer and inner radii of the hollow cylindrical specimen, respectively, and I is the moment of inertia of the specimen, given by $I = \pi(r_o^4 - r_i^4)/4$ ($r_i = 0$ for solid specimens).

Materials

To validate the test fixture design and operation, brittle (borosilicate glass) and quasi-brittle (3D print polymers) materials with different surface conditions were chosen. The borosilicate glass rods were chosen because they exhibit typical brittle failure. However, different surface treatments can affect the strength of a brittle material, as they introduce new stress concentrators, and strengthen or reduce the stress intensity factors of existing stress concentrators [7]. Such microstructural alteration can amplify the stress state at material defects, promoting premature material failure. Hence, the borosilicate rods were subjected to different

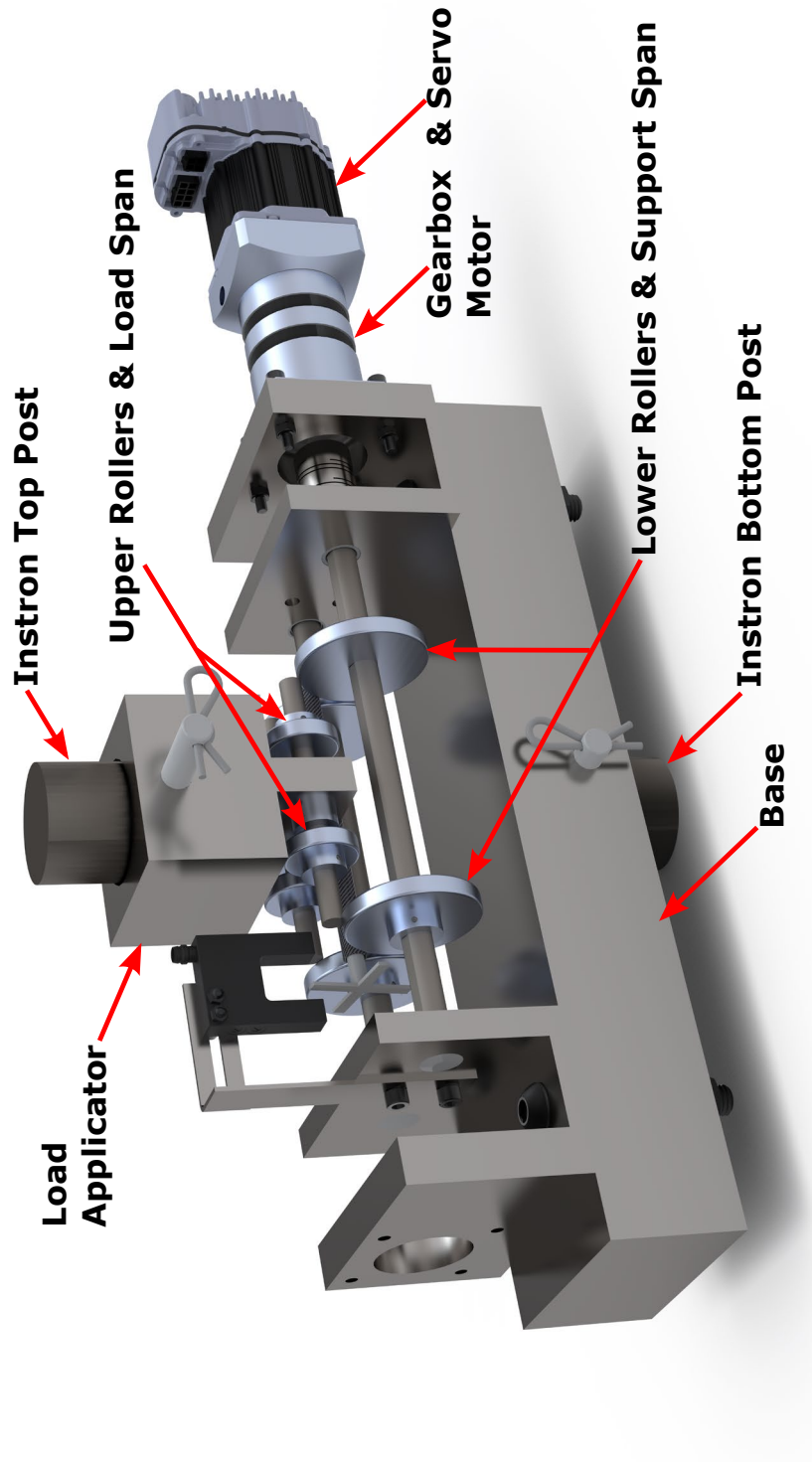


Fig. 1 3D rendering of the rotating four-point bend test fixture

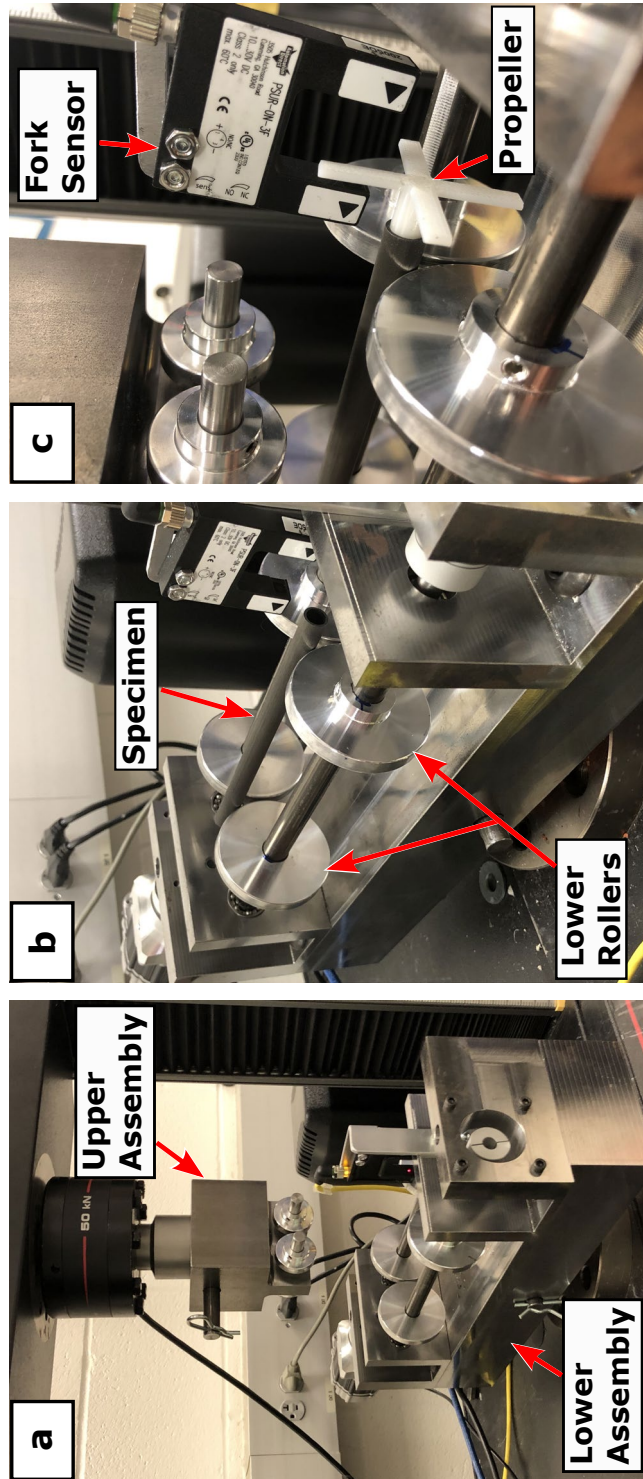


Fig. 2 (a) Upper and lower assemblies mounted on the Instron® frame, (b) Test specimen resting on the lower rollers, and (c) specimen held between the upper and lower rollers. The propeller is attached to the specimen and passes through the fork sensor to measure the rotational velocity

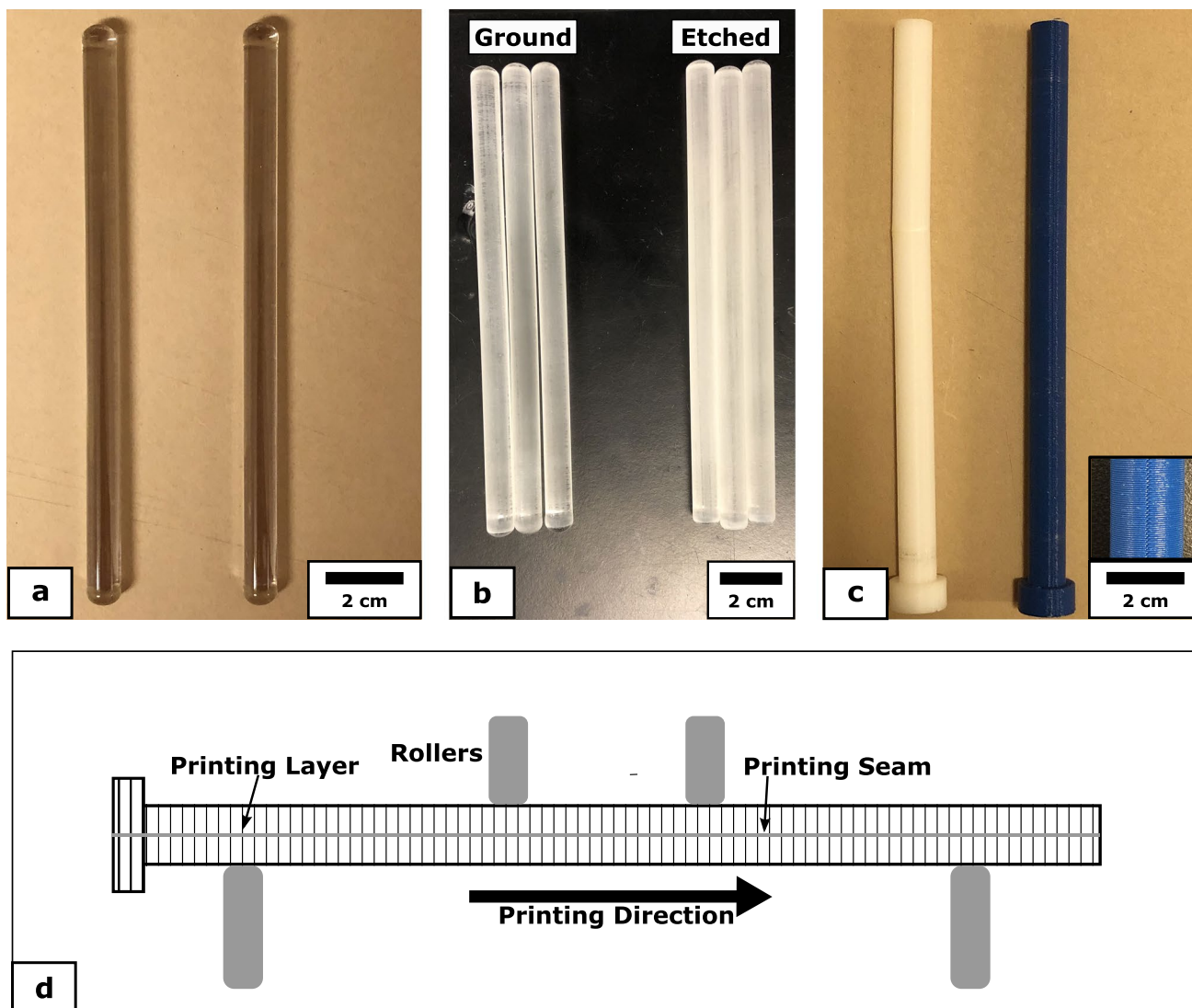


Fig. 3 Representative images of the tested specimens: (a) Untreated glass rods, (b) glass rods with induced surface roughness via grinding, and grinding followed by chemical etching, (c) 3D printed polymer tubes (Z-HIPS in white and Z-ULTRAT in dark blue), (d) a schematic illustrating polymer tube printing layers (gray) and printing direction

surface treatments to verify if the new fixture captured these strength variations.

Although the 3D print polymers typically exhibit ductile failure, the 3D printing process can cause the tubes to fail in a quasi-brittle manner along the interface of the successive 3D-printed layers, similar to delamination in laminar composites [8].

Borosilicate Glass Rods with Different Surface Treatments

Borosilicate type 3.3 glass rods (Borosil® Ltd.) with a diameter of 9 mm and length of 150 mm were prepared with five different surface treatments: (i) untreated (as received); surface ground with a sandpaper of (ii) 60-grit, (iii) 180-grit,

and (iv) 400-grit; and (v) chemically etched after grinding with 60-grit sandpaper¹. All rods were hand-ground for approximately 10 min along their length, and then for approximately another 5 min along their circumference. Surface chemical etching of 60-grit ground specimens was performed by immersing the rods in a buffered oxide etchant (BOE, i.e., 50% water, 43% ammonium fluoride and 7% hydrofluoric acid) for 15 min. The average surface roughness (R_a) resulting from various surface treatments was measured at five different locations using an optical profilometer (Bruker Contour GT-I). Images of untreated rods, ground

¹ Lower grit numbers refer to coarser and larger grits and hence, result in higher surface roughness on the specimens.

rods, and ground and chemically etched rods are shown in Fig. 3(a-b).

3D Printed Polymer Tubes

The 3D printed materials selected for this investigation were proprietary High Impact Polystyrene (Z-HIPS®) and ABS (Z-ULTRAT®) blends, printed using layer plastic deposition printer (Zortrax S.A., model M300 Plus), with a 0.4 mm diameter nozzle. The 3D printed specimens were 150 mm in length and had nominal outer and inner diameters of 9.9 mm and 6.6 mm, respectively. Tubular specimens were chosen over solid specimens for two reasons: (i) hollow specimens can be printed at faster print rates and at lower material costs with reduced print warping compared to printing solid parts of sizable diameter and (ii) to validate the fixture for hollow specimens in addition to solid glass specimens. The filament is 0.4 mm in diameter and the wall thickness of the specimens is ~2.3 mm. Due to the thin wall thickness of the polymer tubes, all layers are solid boundary layers and hence there is no infill pattern. To obtain a circular cross-section we have chosen to deposit the printing filament along the circumferential direction (perpendicular to the tube length), while simultaneously building the tube in the axial direction. Printing specimens with filament orientation along the tube length will not exhibit brittle failure in a flexure test because the printing material is a polymeric wire which is ductile in the intra-layer direction [8]. The circumferential printing orientation promotes brittle failure because the specimen strength is now dependent on the interfacial bond strength between the successive filament layers. Typical 3D printed tubes and a tube printing schematic are shown in Fig. 3(c) and (d), respectively. In Fig. 3(c), a seam is visible on the 3D printed specimen. While this seam is an unavoidable intrinsic defect of the 3D printing process, it was considered advantageous as it served as the critical flaw for the polymer tubes. Specimen failure was observed to initiate from this seam and contributed to the validation of the proposed flexural strength measurement technique. The seam was not observed to affect specimen rotation. The knobs at the bottom end of the tubes are used for positioning the tubes along the outer rollers and do not affect strength measurements.

Results & Discussion

The borosilicate glass rods were tested with a displacement rate of 0.005 mm/s and a rotational speed of 80 rpm, while the polymer tubes were tested with a displacement rate of 0.0125 mm/s and a rotational speed of 125 rpm. The rotational speed was carefully chosen to allow small load increments (to maintain quasistatic loading) while minimizing force fluctuations and fixture vibrations. In general,

Table 1 Surface roughness and flexural strength of borosilicate glass rods

Surface Treatment	Surface Roughness, Ra (nm)	Flexural Strength (MPa)	
		Conventional	Rotational
Literature [10]	N/A	44.12	N/A
Untreated	24.5 ± 3	69.74 ± 6.47	37.11 ± 2.52
400 Grit	692.5 ± 21	37.10 ± 5.49	32.95 ± 1.45
180 Grit	1,634 ± 62	45.30 ± 5.06	26.60 ± 0.99
60 Grit	1,858 ± 31	35.07 ± 2.28	23.96 ± 1.39
60 Grit with chemical etch	3,002 ± 12	54.52 ± 6.83	29.02 ± 1.44

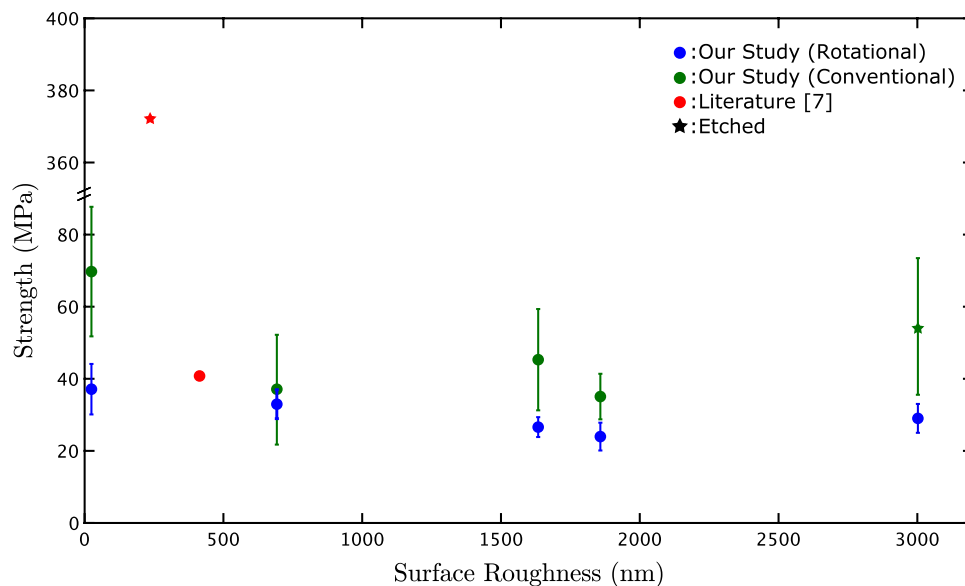
rotational speeds greater than 200 were avoided and the rate of displacement was chosen to minimize fatigue effects in a specimen, i.e., relatively low number of cycles to failure. The tests were conducted until specimen failure occurred. At least five specimens were tested for each specimen type.

Surface Roughness and Failure Analysis of Glass Rods

The surface roughness for glass rods with different surface treatments and the corresponding flexural strength values from the rotating flexure tests are presented in Table 1; Fig. 4. While the untreated rods had a very low surface roughness (only 24.5 ± 3 nm), grinding with 400 grit to 60 grit sandpapers increased the surface roughness by approximately 30 to 80 times, respectively (see Table 1). Furthermore, etching with BOE of the 60-grit ground surface increased the roughness by 120 times compared to the virgin surface. The consequence of this surface roughness is seen in the measured flexural strength values in Table 1. The strength decreased monotonically with increasing surface roughness for the three exclusively ground samples. With decreasing grit number (i.e., larger grit size), deeper grooves with potentially strength limiting cracks were created on the glass surface, which reduced the flexural strength significantly. However, this trend of decreasing strength with increasing surface roughness did not apply to the specimens that were chemically etched following grinding with 60-grit paper. The strength of these rods increased significantly, surpassing even that of the 180-grit ground rods. This result is not surprising, as the chemical etching is known to blunt the sharpness of grinding-induced grooves, thus reducing their stress concentration significantly [9].

As seen in Fig. 4, the flexural strength measured through the rotating bend test is ~16% lower than the values found in literature [10] for a conventional four-point bend test on untreated borosilicate glass. The rotation of the specimen results in every point on the surface of the rod experiencing the state of maximum tension during loading. Hence, a

Fig. 4 Strength of borosilicate glass, from this study (blue: rotational, green: conventional) and literature (red), as a function of surface roughness with error bars corresponding to 95% confidence intervals



critical surface flaw that is more severe than that activated in a conventional flexure test (i.e., without rotation) may have been activated during the rotating flexural test. The activation of the most critical flaw is not guaranteed in the conventional test unless the critical flaw is already on the line experiencing maximum tensile stress, which is less likely.

For the borosilicate glass rods with different surface treatments, it is noted that the rotating flexure data shows lower strength measurements as compared to literature [7] and the conventional flexure data from this study, with the exception of the specimens with 180-grit treatment. Lower flexural strengths for the rotating bend test can be attributed to two factors: (i) higher loading rates used in [7] where the loading rate was 0.7 MPa/s compared to 0.18 MPa/s in our study; typically, higher loading rates results in higher strength in brittle materials [2, 3], and (ii) higher probability of exposing the most critical flaw to tension in the rotating flexure test compared to the conventional flexure test results in lower strength.

To validate that specimen rotation was the primary factor to critical flaw activation and hence, lower failure loads, conventional four-point bend tests were performed using the same test fixture for the five glass samples, without specimen rotation. The remaining test conditions for the conventional tests were the same as that for the rotational tests. It is noted that, for any given surface treatment, the conventional flexural strength is greater than the rotational flexural strength. The conventional strengths being higher than the rotational strengths is expected because without specimen rotation, the critical flaw may not be activated, i.e., experience maximum tensile stress. While the conventional flexural strengths followed a similar strength trend with respect to surface roughness as compared to the rotational flexural strengths, the trend was not exact (Fig. 4). Most notably, the conventional

flexural strength for the 400-grit specimens was less than the conventional flexural strength of the 180-grit specimens (Table 1). This difference highlights the uncertainty associated with conventional four-point bend flexural strength tests and supports the developed test fixture's ability to measure a specimen's true flexural strength.

To confirm that the specimen failure occurs due to flexural loading, the fracture path and surface of each specimen are studied. Figure 5(a) shows the classic compression curl fracture of a brittle cylindrical bar subjected to quasi-static flexural loading. The fracture initiates on the tensile side and propagates perpendicular to the tensile axis into the specimen. As the crack enters the compressive zone, it slows down and changes direction to propagate parallel to the direction of compression [11, 12]. This mode of crack propagation parallel to the compression axis is well known in brittle fracture literature [13, 14]. Every glass specimen tested with the rotating flexure fixture exhibited this compression curl and have similar fracture surface features, shown in Fig. 5(b-c), which include (i) a fracture origin located on the tensile side, (ii) a fracture mirror around the fracture origin, (iii) Wallner lines [15] indicating the direction of crack propagation, and (iv) the compression curl. These features of fracture surfaces are consistent with the features observed in conventional quasistatic bend test failure surfaces [11]. The presence of the above listed features on the fracture surfaces of the glass rods tested with the rotational four-point bend test fixture confirms that failure occurred primarily due to flexural loading, despite the specimen rotation. Additionally, it is noted that the fracture origins are near the surface of the specimens, indicating that failure was not due to an internal bulk defect, but rather due to a surface defect (critical flaw) induced during specimen preparation. While failure occurred in the gage section of

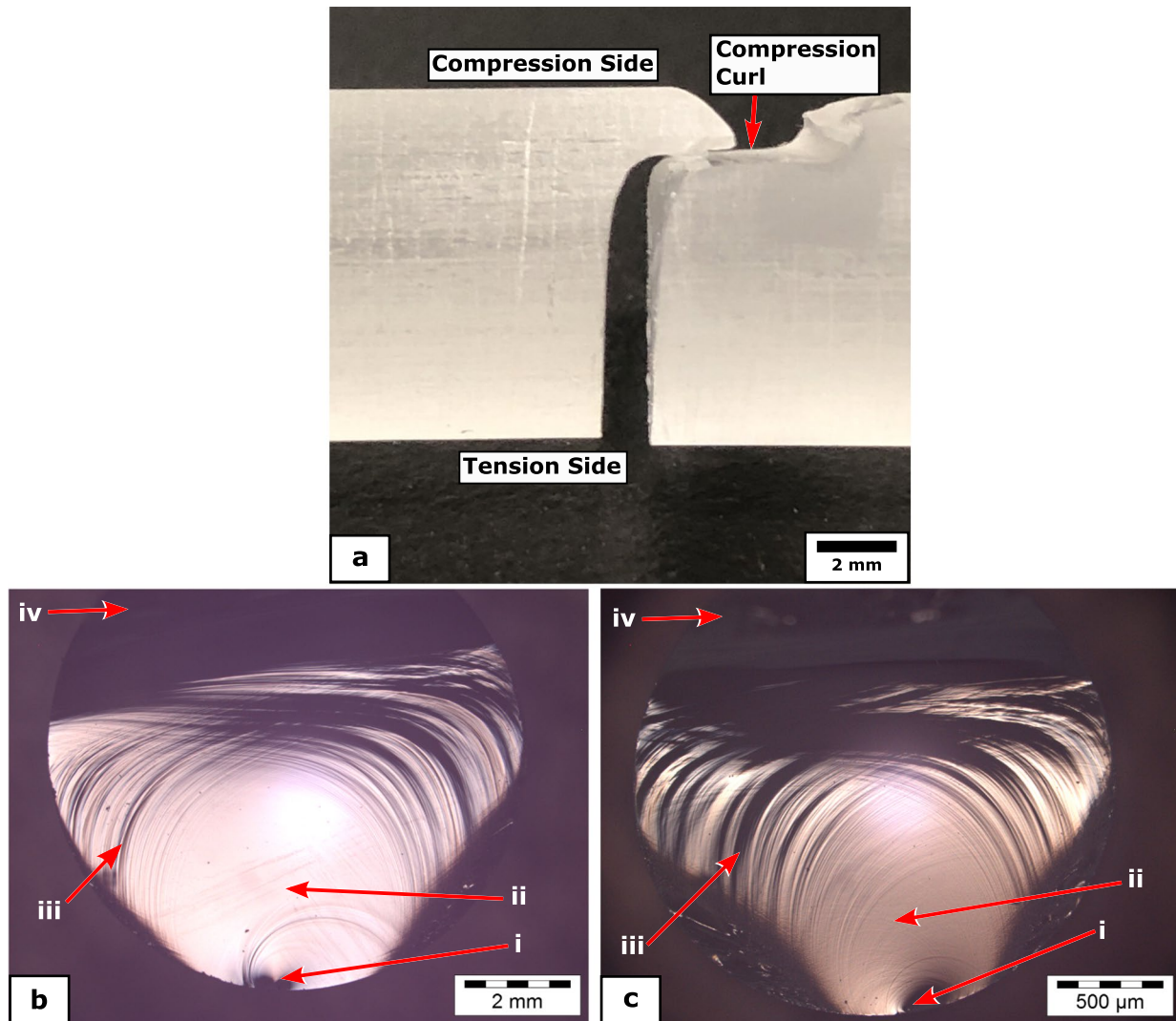


Fig. 5 Representative fracture profiles for borosilicate glass rods following four-point bending. **(a)** Fracture path showing compression curl. **(b-c)** Failure surfaces showing (i) fracture origin, (ii) fracture mirror, (iii) Wallner lines, and (iv) compression curl for **(b)** untreated and **(c)** 400-grit specimen

each specimen, the failure analysis clearly suggested bending dominated failure. The effect of friction on specimen torsion was investigated to determine its role in specimen failure. The specimens and rollers have circular geometries, therefore the friction interaction between these two surfaces can be modeled as rolling resistance between two cylinders. Torsion from rolling friction arises from force differentials between two sets of rollers.

Calculations that support the negligible effect of torsion on specimen failure are presented in the following by considering the worst case scenario. The highest torsion would be produced when there is a maximum rotation differential between the inner and outer rollers, and the applied maximum load is used to calculate the torque (T) due to friction between the

rollers and the specimens. The equations for torsional shear stress and bending stress, respectively, are given by

$$\tau = \frac{Tr}{J} = \frac{(F\mu r)r}{J} \quad (2)$$

$$\sigma = \frac{My}{I} = \frac{(Fd)r}{I} \quad (3)$$

where F is the force on each roller (equal to a quarter of the total applied load as there are 4 bottom rollers supporting the specimen), μ is the friction coefficient between the roller and the specimen, r is the radius of the specimen, and $d = 0.04\text{m}$ is the distance between an adjacent inner and outer roller. I and J are the planar and polar second moments of area,

Table 2 Surface roughness, flexural and tensile strengths of 3-D printed specimens

Filament material	Surface roughness, Ra (nm)	Flexural strength, σ_f (MPa)			Tensile strength, σ_t (MPa)	$\frac{\sigma_f}{\sigma_t}$
		Literature	This study			
			Conventional	Rotational		
Z-HIPS®	17,932 ± 641	29.3 [16]	26.92 ± 0.35	17.86 ± 0.92	4.09 ± 0.19	4.37
Z-ULTRAT®	20,892 ± 812	54 [17]	27.43 ± 1.02	18.94 ± 1.04	3.98 ± 0.22	4.76

respectively. For objects that have rotational symmetry (the cylinders discussed here), $I = 2J$. Hence, dividing equations (2) by (3) results in

$$\frac{\tau}{\sigma} = 3.125\mu r \quad (4)$$

which is the ratio of the torsional shear stress to the bending stress. Using a conservative friction coefficient value of $\mu = 0.7$ for the glass specimen – metal roller interface [16], and the radius of the tested borosilicate specimens ($r = 4.5$ mm), the induced shear stress due to torsion was calculated to be 0.0098σ , i.e., less than 1% of the bending stress. These calculations represent the worst-case scenario, and hence, we can conclude that the torsion resulting from friction has a negligible effect on the stress state in the specimen. This was also confirmed by observing the failure patterns on glass rods which showed typical bending fracture (perpendicular to the axis of the specimen) followed by a compression curl (see Fig. 5(a)).

The similarities between the fracture surface features and the trend of strength values observed in this study, and that observed in similar studies on borosilicate glass with varying surface treatments, provide evidence that the tests performed with the new rotating four-point bend fixture yield a better measure of the flexural strength for a brittle material like borosilicate glass.

Failure Analysis of 3D Printed Polymer Tubes

The average flexural strengths of 3D printed Z-HIPS® and Z-ULTRAT® tubular specimens determined from the rotating bend test are shown in Table 2. It can be seen that there is a large disparity between the literature values [17, 18] and our experimental measurements of flexural strength. This disparity is attributed to the differences in the printing orientation in relation to the loading direction. It is well known that printing orientation has a strong influence on material properties and that 3D printed parts exhibit highly anisotropic behavior [8, 19, 20]. In general, the strength of each 3D-printed layer (i.e., the intra-layer strength) is much higher than the interfacial strength between adjacent layers (i.e., the inter-layer strength). The material strength values reported in literature are based on bending tests of specimens with the layers orientated perpendicular to the

direction of loading. In this orientation, the strongest orientation of the material is parallel to the direction of the tensile stress (i.e., along the specimen length). However, for the tubular specimens studied here, the layers are oriented perpendicular to the specimen length, along the circumferential direction. Hence, the direction of tensile stress during four-point bending is parallel to the weakest orientation of the specimen.

Figure 6 illustrates the failure mode in these 3D-printed tubes. The failure occurs on a plane perpendicular to the specimen axis. The higher magnification insets show the failure planes between successive print layers. As the printing orientation is the same for both materials, the failure strength is strictly controlled by the interfacial layer strength which appears to be comparable for both 3D-print materials. For each specimen, failure was observed to originate at the printing seam, demonstrating the fixture's ability to consistently induce failure at a specimen's weakest point.

To verify the validity of the results from the rotating four-point bend tests, the flexural strength was compared to the inter-layer tensile strength of the material. Planar dog-bone shaped specimens were printed with the layer orientation perpendicular to the tensile loading direction. Uniaxial tensile tests were performed on five specimens per material, following the procedure in ASTM D638-Type I [21], with a displacement rate of 0.0833 mm/s (resulting in a strain rate of $1.167 \times 10^{-3} \text{ s}^{-1}$). Like the tubular specimens, the dog bone specimens failed along the interface between two 3D-print layers, as seen in Fig. 7, and the tensile strength of the two specimens are nearly the same (see Table 2). This tensile strength can be deemed to be the interfacial bond strength of the layers. The similarity in inter-layer strength of the two materials is significant as it supports the previous hypothesis that the failure of the tubular specimen under flexural loading was primarily governed by the inter-layer strength, and therefore that the flexural strengths of both the tubes should be similar in value as well.

The tensile strength (σ_t) of these 3D printed tubes is much lower than their flexural strength (σ_f), and the ratio σ_f/σ_t for both materials is also presented in Table 2. This ratio is in accordance with the literature [22, 23]; for typical brittle materials these values are generally within the range of 1–5, with a ratio of 1.25 for alumina [23], and 2.27 for borosilicate glass [24], and 3.63 for zirconia [23].

Fig. 6 Inter-filament failure of (a) Z-HIPS specimen and (b) Z-ULTRAT specimens following rotational four-point bend tests

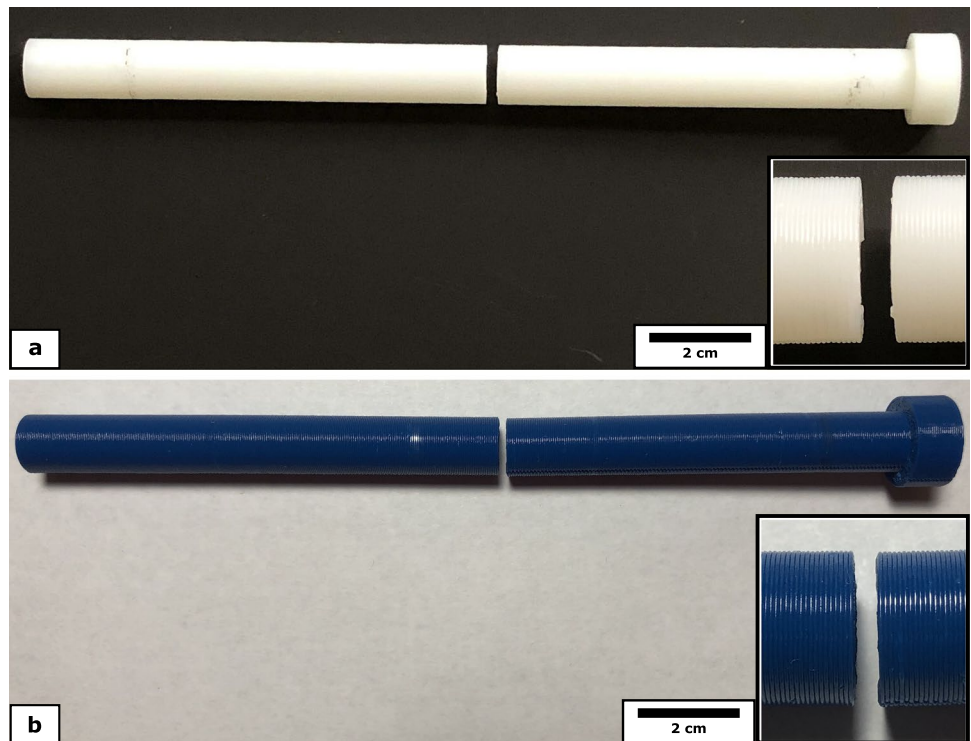
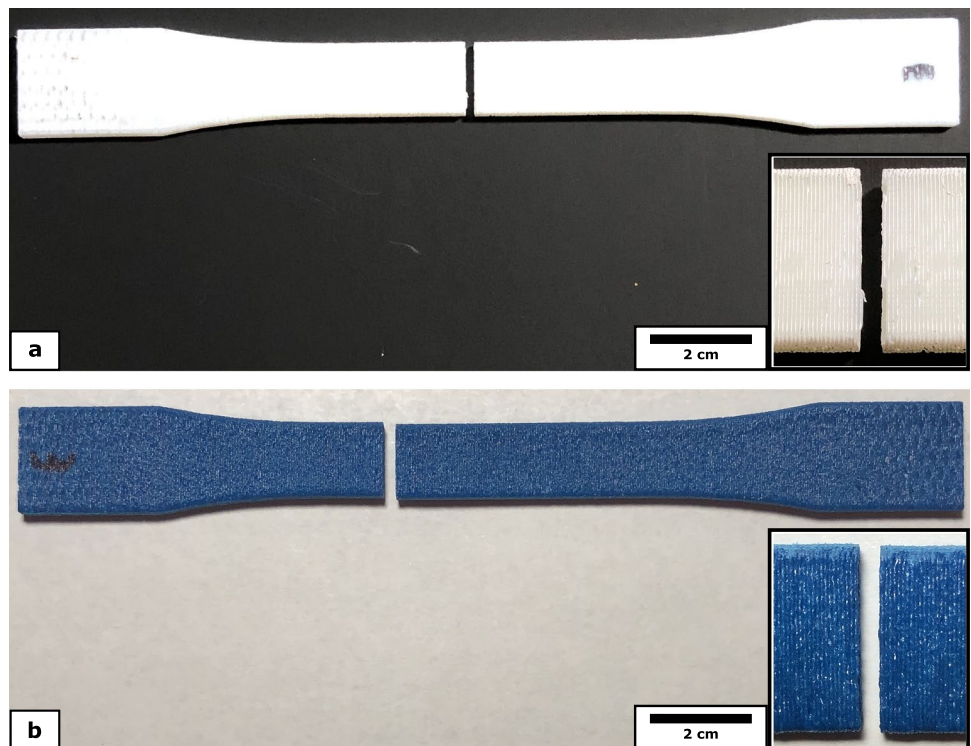


Fig. 7 Inter-filament failure of (a) Z-HIPS® and (b) Z-ULTRAT® dog-bone specimens following uniaxial tensile tests



The corresponding ratios for the 3D printed materials also fall within this range. This result, along with the visual evidence (Figs. 6 and 7), supports the assumption that the polymer tubes failed in a brittle manner.

Similar to the borosilicate samples, conventional flexural strength tests were performed with the new test fixture (without rotation) for the Z-HIPS® and Z-ULTRAT® samples. The conventional tests parameters were identical

to the rotational tests, except that there was no specimen rotation. Similar to the borosilicate samples, the polymer tube's conventional flexural strengths were greater than the rotational flexural strengths (Table 2). This difference in measured strengths can also be attributed to the critical flaws of the polymer tubes not being activated in the tested orientation.

Conclusions

A novel rotating four-point bend test fixture was developed to measure the true flexural strength of brittle materials. The brittle and quasi-brittle specimens tested using this rotational fixture failed at lower strength values than those tested without rotation, due to critical flaw activation promoted via specimen rotation. The presence of compression curls and fracture surface features validate that flexural failure was achieved near the surface of the glass rods.

Additionally, it was observed that, for the glass rods, flexural strength decreased with increasing surface roughness. However, etching a ground rod resulted in an increase in flexural strength compared to the ground specimens, due to the reduction in stress concentration at the grinding induced crack tips. Both these trends are supported by literature, thereby adding validity to the new test methodology.

The quasi-brittle polymer specimens failed at lower strengths than the values reported by the manufacturer. However, this result can be primarily attributed to variations in printing orientation between the test specimens. Furthermore, the printing orientation chosen for our study is posited to contribute to the measured strength similarities between the polymer materials tested. Tensile tests confirmed that failure occurred at the interfaces between successive print layers.

The results of this study emphasize the influence of critical flaws in brittle materials, and hence the importance of accurate flexural strength measurement techniques for brittle materials. Conventional four-point bend tests over-estimate the flexural strength of brittle materials as the critical flaw is unlikely to be activated due to a limited portion of the specimen surface experiencing the maximum tensile stress. Rotating the specimen during flexural testing is crucial to activating its critical flaw and measuring the true flexural strength of a brittle material.

Acknowledgements The research was performed under Department of Energy (DOE) Nuclear Energy University Programs (NEUP) grant number DE-NE0008773 to University of Florida.

Declarations

The authors declare that they have no known competing financial interests or personal relationships that could have appeared to influence the work reported in this paper.

References

- Osés C, Toher C, Curtarolo S (2020) High-entropy ceramics. *Nat Rev Mater* 5:295–309. <https://doi.org/10.1038/s41578-019-0170-8>
- Subhash G, Ghosh D, Awasthi A (2021) Dynamic response of advanced ceramics. Wiley, Hoboken
- Bavdekar S, Subhash G (2021) Failure mechanisms of ceramics under quasi-static and dynamic loads: overview. *Handbook of damage mechanics*. Springer New York, New York, pp 1–29
- Griffith AA (1921) The phenomena of rupture and flow in solids. *Philos Trans R Soc A Math Phys Eng Sci* 221:163–198. <https://doi.org/10.1098/rsta.1921.0006>
- Vargas-Gonzalez L, Speyer RF, Campbell J (2010) Flexural strength, fracture toughness, and hardness of silicon carbide and boron carbide armor ceramics. *Int J Appl Ceram Technol* 7:643–651. <https://doi.org/10.1111/j.1744-7402.2010.02501.x>
- ASTM (2018) ASTM C1421-18, Standard test methods for determination of fracture toughness of advanced ceramics at ambient temperature. ASTM International, West Conshohocken
- Nie X, Chen WW, Wereszczak AA, Templeton DW (2009) Effect of loading rate and surface conditions on the flexural strength of borosilicate glass. *J Am Ceram Soc* 92:1287–1295. <https://doi.org/10.1111/j.1551-2916.2009.03019.x>
- Cantrell JT, Rohde S, Damiani D et al (2017) Experimental characterization of the mechanical properties of 3D-printed ABS and polycarbonate parts. *Rapid Prototyp J* 23:811–824. <https://doi.org/10.1108/RPJ-03-2016-0042>
- Spierings GACM (1993) Wet chemical etching of silicate glasses in hydrofluoric acid based solutions. *J Mater Sci* 28:6261–6273. <https://doi.org/10.1007/BF01352182>
- Bouras N, Madjoubi MA, Kolli M et al (2009) Thermal and mechanical characterization of borosilicate glass. *Phys Procedia* 2:1135–1140. <https://doi.org/10.1016/j.phpro.2009.11.074>
- Quinn GD (2016) NIST Recommended practice guide fractography of ceramics and glasses. Gaithersburg, MD
- Tsirk A (2014) Fractures in knapping. Archaeopress Publishing Ltd, Gloucestershire
- Horii H, Nemat-Nasser S (1985) Compression-induced micro-crack growth in brittle solids: Axial splitting and shear failure. *J Geophys Res* 90:3105. <https://doi.org/10.1029/jb090ib04p03105>
- Ashby MF, Hallam (Née Cooksley) SD (1986) The failure of brittle solids containing small cracks under compressive stress states. *Acta Metall* 34:497–510. [https://doi.org/10.1016/0001-6160\(86\)90086-6](https://doi.org/10.1016/0001-6160(86)90086-6)
- Wallner H (1939) Linienstrukturen an Bruchflächen. *Z Phys* 114:368–378. <https://doi.org/10.1007/BF01337002>
- Buckley-lewis DH (1973) Friction behavior of glass and metals in contact with glass in various environments. Nasa Technical Note
- Zortrax SA (2020) Z-HIPS Technical Data. [zortrax.com/filaments/z-hips/](https://www.zortrax.com/filaments/z-hips/). Accessed 6 Oct 2021
- Zortrax SA (2020) Z-UltraT Technical Data. [zortrax.com/filaments/z-ultrat/](https://www.zortrax.com/filaments/z-ultrat/). Accessed 6 Oct 2021
- Ahn S, Montero M, Odell D et al (2002) Anisotropic material properties of fused deposition modeling ABS. *Rapid Prototyp J* 8:248–257. <https://doi.org/10.1108/13552540210441166>

20. Bellini A, Güçeri S (2003) Mechanical characterization of parts fabricated using fused deposition modeling. *Rapid Prototyp J* 9:252–264. <https://doi.org/10.1108/13552540310489631>
21. ASTM (2014) Standard test method for tensile properties of plastics. ASTM International, West Conshohocken
22. Syrlybayev D, Zharylkassyn B, Seisekulova A et al (2021) Optimisation of strength properties of FDM printed parts—A critical review. *Polym (Basel)* 13. <https://doi.org/10.3390/polym13101587>
23. Engineering ToolBox (2008) Ceramic materials properties. https://www.engineeringtoolbox.com/ceramics-properties-d_1227.html
24. Alarcon OE, Medrano RE, Gillis PP (1994) Fracture of glass in tensile and bending tests. 25:961–968. <https://doi.org/10.1007/BF02652271>

Publisher's Note Springer Nature remains neutral with regard to jurisdictional claims in published maps and institutional affiliations.